

Kelvin-Helmholtz versus Tearing Instability: What Drives Turbulence in Stochastic Reconnection?

GRZEGORZ KOWAL,¹ DIEGO A. FALCETA-GONÇALVES,¹ ALEX LAZARIAN,² AND ETHAN T. VISHNIAC³

¹*Escola de Artes, Ciências e Humanidades
Universidade de São Paulo
Av. Arlindo Béttio, 1000 – Vila Guaraciaba
CEP: 03828-000, São Paulo - SP, Brazil*

²*Department of Astronomy
University of Wisconsin,
475 North Charter Street,
Madison, WI 53706, USA*

³*Department of Physics & Astronomy
Johns Hopkins University
3400 N. Charles Street
Baltimore, MD 21218, USA*

Submitted to ApJ

Abstract

Over the last few years it became clear that turbulent magnetic reconnection and magnetized turbulence are inseparable. It was not only shown that reconnection is responsible for violating the frozen-in condition in turbulence, but also that stochastic reconnection in 3D generates turbulence by itself. The actual mechanism responsible for this driving is still unknown. Processes such as turbulent tearing mode or Kelvin–Helmholtz, among other plasma instabilities, could generate turbulence from irregular current sheets. We address the nature of the driving mechanism for this process and consider a relative role of tearing and Kelvin–Helmholtz instabilities for the process of turbulence generation. In particular, we analyze the conditions for development of these two instabilities within three-dimensional reconnection regions. We show that both instabilities can excite turbulence fluctuations in reconnection regions. However, tearing mode has a relatively slow growth rate, and at later times it becomes partially suppressed by the transverse component of the magnetic field, generated during the growth of turbulent fluctuations. On the contrary, the Kelvin–Helmholtz instability establishes quickly in the outflow region, and at later times it dominates the turbulence generation compared to the contribution from tearing mode. Our results demonstrate that the tearing instability is subdominant compared to the Kelvin–Helmholtz instability in terms of generation of turbulence in the 3D reconnection layers and therefore the self-driven reconnection is turbulent reconnection with tearing instability being important only at the initial stage of the reconnection.

Keywords: magnetic reconnection — turbulence — magnetohydrodynamics (MHD) — methods: numerical

1. INTRODUCTION

Magnetic reconnection is a fundamental problem essential for understanding the magnetohydrodynamic (MHD) flows. Within such flows magnetic flux tubes

cross each other and therefore the properties of the flow depend on whether the tubes can or cannot cross each other.

The answer that follows from the Sweet–Parker theory of magnetic reconnection (Parker 1957; Sweet 1958) is that in typical astrophysical situations the magnetic flux tubes cannot reconnect and change the magnetic field topology. Indeed, the Sweet–Parker reconnection

rate is $V_{\text{rec,SP}} \approx V_A S^{1/2} \ll V_A$ with $S = LV_A/\eta$ being the Lundquist number, where L is a scale of the reconnecting flux tube and V_A is the Alfvén speed. Given the large scales of magnetic fields involved in astrophysical flows and the highly conductive nature of astrophysical plasmas, it is obvious that S is so large that the rates predicted by the Sweet–Parker mechanism are absolutely negligible. This, however, is in gross contradiction with observational data, e.g., the data on Solar flares. The Sweet–Parker reconnection is an example of a slow reconnection, while one requires much faster reconnection to explain observations. Formally, the fast reconnection is the reconnection that does not depend on S or, if depends, depends on it logarithmically.

For years the fast reconnection research was focused on the X-point reconnection, i.e. the reconnection at which magnetic field is brought at a sharp angle in the reconnection zone. This is opposed to the Sweet-Parker reconnection which is an example of the Y-point reconnection. The X-point reconnection was proposed by Petschek (1964) and required that the inflow and outflow of the matter into reconnection zone are comparable. Indeed, the slow rate of reconnection with Y-point can be viewed as a direct consequence of the disparity of the scale of astrophysical inflow of the fluid and the scale of outflow determined by microphysics, i.e., the resistivity or plasma effects, the latter, however, challenged by Lazarian & Vishniac (1999, henceforth LV99).

The most significant point of the LV99 theory was that in the presence of the 3D turbulence, the reconnection outflow is determined by the magnetic field wandering and the width of the outflow is the function of turbulence intensity rather than the resistivity of plasma effects¹. The predicted by the LV99 theory dependence of the reconnection rate on the level of turbulence was successfully tested in the numerical studies of Kowal et al. (2009, 2012). More recently, these predictions received an additional support from relativistic MHD simulations by Takamoto et al. (2015). The most important consequence of the LV99 theory, contrary to all the previous theories of fast reconnection, was the prediction

¹ The LV99 proposal was radically different from earlier suggestions of enhancing the reconnection rate by turbulence. For instance, Jacobson & Moses (1984) considered effect of turbulence on micro-scales by increasing Ohmic resistivity. Obviously, this could provide the change of the Sweet-Parker rate only by an insignificant factor. Similarly, 2D simulations of turbulence in Matthaeus & Lamkin (1985, 1986) could not shed light on the actual 3D physics of magnetic reconnection. Indeed, the component of magnetic field responsible for the wandering in LV99 model is the Alfvénic mode. This mode is absent in 2D simulations. Thus the authors were appealing to the X-points that are produced by turbulence.

that the reconnection does not require any special settings, but happens everywhere in turbulent media. As a result, this violates flux freezing in astrophysical fluids, which are generically turbulent (Eyink 2011; Eyink et al. 2011). This remarkable break down of the classical magnetic flux freezing (Alfvén 1942) theorem was numerically demonstrated in (Eyink et al. 2013)².

Turbulence can be both externally driven, as it is testified from the observations of the ISM and molecular clouds (see Armstrong et al. 1995; Padoan et al. 2009; Chepurnov & Lazarian 2010; Chepurnov et al. 2015), but it can be also driven by the reconnection process as first discussed in LV99 and further elaborated in Lazarian & Vishniac (2009). The first numerical study of magnetic reconnection induced by turbulence that is generated by reconnection were performed in Beresnyak (2013) with an incompressible code, and later in Oishi et al. (2015) and Huang & Bhattacharjee (2016) taking into account compressibility. A detailed numerical study of reconnection with self-generated turbulence was performed in Kowal et al. (2017).

One of the most important questions of the current research in 3D reconnection faces the nature of turbulence in the reconnection events. Our earlier study in Kowal et al. (2017) demonstrated that the turbulence generated in the reconnection events follows the Goldreich–Sridhar statistics (Goldreich & Sridhar 1995). However, an open issue is related to the driving mechanism of the observed turbulent motions. The literature has suggested that tearing modes, plasmoid instabilities, and shear-induced instabilities could mediate the energy transfer from coherent to turbulent flows. The issue of the relative importance of different driving processes has not been explored quantitatively.

In our numerical experiments we do not identify tearing modes, although filamentary plasmoid-like structures are present. Visual inspection shows, however, that the filling factor of these is small. Sheared flows, on the other hand, are present around and within the whole current sheet. As the field lines reconnect, the $\vec{v} \times \vec{B} + \vec{E}$ force increases, accelerating the plasma and creating the current sheet. This process is, in three dimensions, patchy and bursty. Therefore, the accelerated flows are strongly sheared. The statistical importance of these burst flows is large, as already shown in the previous work (Kowal et al. 2017), as we compared the velocity anisotropy of reconnecting events to that of decaying

² The violation of flux freezing in turbulent fluids entails an important effect of reconnection diffusion that has big consequences, changing the paradigm of magnetically controlled star formation (see Lazarian 2005; Santos-Lima et al. 2010; Lazarian et al. 2012).

turbulence without the reversed field. Kelvin–Helmholtz instability due to the sheared velocities in reconnecting layers has already been conjectured as possible origin of turbulence by Beresnyak (2013). In Kowal et al. (2017), we provided the solid evidence for the self-generated turbulence driven by the velocity shear. Here we perform a proper analysis of the growth-rates of such instabilities.

Velocity shear is a global process that occurs in regular magnetized and unmagnetized fluids. The nonlinear evolution of the related instabilities, such as Kelvin–Helmholtz instability, is known to be one of the main contributors to the energy transfer between wave modes, i.e., the energy cascade. If the energy cascade in reconnection layers is led by similar mechanisms, it is straightforward to understand why the statistics observed resemble those of Kolmogorov-like turbulence, and Goldreich–Sridhar anisotropy scaling. In other words, our claim is that the turbulent onset and cascade in reconnection is not different to those found in regular MHD and hydrodynamic systems.

In what follows we provide the analysis of Kelvin–Helmholtz and tearing instabilities and define the conditions for their suppression in §2, describe our approach and numerical simulations in §3, compare the rates of the two instabilities at different times in §4, discuss and state our conclusions in §5 and §6.

2. ANALYZED INSTABILITIES

2.1. Tearing Mode Instability

In the following analysis we considered two possible instabilities, namely tearing mode instability (Furth et al. 1963), which naturally develops in a thin elongated current sheet, and Kelvin–Helmholtz instability (e.g. Chandrasekhar 1961), which could result from the local shear produced by the outflows from reconnection sites. Both instabilities are able to generate turbulence near current sheets, however, there is no clear answer which one is responsible for or dominates the generation of turbulence from stochastic reconnection, i.e. the reconnection without an externally imposed turbulence and resulting from a weak initial plasma irregularities.

Following the analytic work by Furth et al. (1963), which investigated the finite-resistivity instabilities of a sheet pinch, we know that the tearing instability develops under condition $k\delta < 1$, where k is the perturbation wavelength (in the sheet plane) and δ is the current sheet half-width (see Table 1 in Furth et al. 1963). When this condition is satisfied, the growth rate of the instability $\omega\tau_A$ within one Alfvén time $\tau_A = L/v_A$, where L is the current sheet length and $v_A = |\vec{B}|/\sqrt{\mu_0\rho}$ is the Alfvén

speed, is given by

$$\omega\tau_A = p \frac{\tau_A}{\tau_R} = \left(\frac{2S_\delta}{\pi k\delta}\right)^{2/5} S_\delta^{-1} = \left(\frac{2}{\pi}\right)^{2/5} (k\delta)^{-2/5} S_\delta^{-3/5}, \quad (1)$$

where $p = \omega\tau_R = \left(\frac{2S_\delta}{\pi k\delta}\right)^{2/5}$ is the growth rate in terms of the resistive time scale τ_R (as provided in Furth et al. 1963), $S_\delta = \frac{v_A\delta}{\eta} = \frac{v_AL}{\eta L} = S_L \frac{\delta}{L}$ is the specific Lundquist number related to δ . The regular Lundquist number $S_L = v_AL/\eta$ is typically much larger than unity, e.g. $S_L \approx 10^3 - 10^4$ in numerical simulations and $S_L \gg 10^9$ in astrophysical plasmas. Also, the current sheet thickness is typically much smaller than its length, i.e. $\frac{L}{\delta} \gg 1$. These conditions indicate that both, in numerical simulations and astrophysical plasmas, tearing instability shall be common. However, the tearing instability is a subject to suppression under some circumstances, in particular in the presence of turbulence. For instance, Somov & Vernet (1993) performed an analytic derivation of the instability in the presence of the transverse component of magnetic field, which could be easily generated by turbulence. They have shown that the expression for the growth rate, once the transverse component is taken into account, changes to

$$(\omega\tau_A)^5 = \left(\frac{2}{\pi}\right)^2 (k\delta)^{-2} S_\delta^{-3} - \xi^2 S_\delta (\omega\tau_A)^4, \quad (2)$$

where $\xi = B_n/B$ is the ratio of the transverse component of magnetic field to the reconnecting one. It can be seen from the equation above, that for $\xi > S_\delta^{-3/4}$, the tearing instability can be partially or completely stabilized. Moreover, the turbulence shearing should destroy the tearing instability, i.e., if the rate v_l/l is larger than the tearing instability rate, the instability should not appear.

2.2. Kelvin–Helmholtz Instability

In the presence of a velocity shear, the Kelvin–Helmholtz instability can develop. Following Chandrasekhar (1961), we can write its growth rate for incompressible flow as

$$\omega\tau_A = 2\pi k \sqrt{\frac{1}{4} \frac{\Delta U^2}{v_A^2} - 1}, \quad (3)$$

where ΔU is the shear velocity, i.e. the change of velocity in its perpendicular direction, v_A is the Alfvén speed and k is the wave number of the perturbation. Once the compressibility is taken into account (see Miura & Pritchett 1982), the instability condition changes to

$$\omega^2 = (k_x^2 + k_y^2) - \frac{1}{4} k_y^2 \frac{\mathcal{M}_s^2 \mathcal{M}_A^2}{\left(\mathcal{M}_A^2 + \mathcal{M}_s^2 - \frac{4(\vec{k}\cdot\vec{B})^2}{k_y^2}\right)}, \quad (4)$$

where $\mathcal{M}_s = \Delta U/a$ and $\mathcal{M}_A = \Delta U/v_A$ are sonic and Alfvénic Mach numbers related to the shear strength, respectively, a is the sound speed, and k_x and k_y are the wave numbers of perturbation in two directions perpendicular to the shear. The analysis in [Miura & Pritchett \(1982\)](#) has shown, that Kelvin–Helmholtz instability is completely suppressed for $\mathcal{M}_s > 2$ or $\mathcal{M}_A < 2$. We should stress, that these numbers are related to ΔU and not to the absolute value of velocity. However, it is important to notice that even though the system may be strongly magnetized overall, in the regions where reconnection occurs the local degree of magnetization decreases considerably, allowing the growth of KH-unstable modes. Moreover, if the direction of the perturbation propagation is perpendicular to the local magnetic field, the stabilization effect of the magnetic field is negligible.

3. METHODOLOGY AND MODELING

3.1. Numerical Simulations

In this work we analyze numerical simulations obtained in studies on the statistics of the reconnection-driven turbulence, presented in [Kowal et al. \(2017\)](#). The simulations were done in a 3D domain with physical dimensions $1.0 \times 4.0 \times 1.0$ using adaptive mesh with the effective grid size $h = 1/1024$ (the same along each direction), by solving the isothermal compressible magnetohydrodynamic equations using a high-order shock-capturing Godunov-type code AMUN³. The magnitude of the initial X -component of magnetic field was set to 1.0 with opposite signs above and below the XZ plane at $y = 0$. A guide field, along the Z direction was also set with a uniform value 0.1. Density was set to 1.0 in the whole computational domain initially. The initial velocity perturbation with a random distribution of directions and small amplitude was set in the region $y \leq 0.1$. For analysis here, we have selected models with sound speed $a = 1.0$ ($\beta = 2.0$) only. For more details about the numerical setup, boundary conditions and methods please refer to [Kowal et al. \(2017\)](#). In all these models we did not set explicit viscosity and resistivity. In addition, we performed one numerical simulation of stochastic reconnection with sound speed $a = 1.0$ and finite viscosity ν and resistivity η , both equal to 10^{-5} , in order to control better the effects of numerical diffusion. The additional model was ran with the effective cell size $h = 1/1024$ up to about $t = 7.0$.

3.2. Shear Detection in Vector Fields

³ The code is freely available at <http://amuncode.org>

In order to detect the locations of current sheet we analyze a quantity which is correlated with the local change of the polarization of magnetic field, or simply magnetic shear. There are several techniques proposed in the literature to determine locations where the reconnection takes place. The most straightforward is the amplitude of current density $|\vec{J}|$. We can also use the magnetic shear angle, i.e. the rotation of the magnetic field vector across the current sheet, or the Partial Variance of Increments method (PVI) which measures the variation of the magnetic field across the current sheet (see [Greco et al. 2008](#); [Servidio et al. 2011](#)). Similarly, for the velocity shear, we can consider, for example, the vorticity $\vec{\omega} = \nabla \times \vec{v}$ as the shear detector. In this work we analyze the local maximums of the euclidean norm of the shear rate tensor $S_{ij} = \partial u_i / \partial x_j + \partial u_j / \partial x_i$, $S = \|S_{ij}\| \equiv \sqrt{\sum_{ij} S_{ij}^2}$, where $x_i, x_j \in \{x, y, z\}$ and \vec{u} means either \vec{B} or \vec{v} , depending on the analyzed instability. Clearly, $S = S(x, y, z)$ is a function of position.

Our algorithm to determine the local geometry of the shear consists of the following steps:

1. At each domain point (x, y, z) (e.g. cell) we calculate the 2^{nd} order partial derivatives of $S(x, y, z)$ along each direction. If at least one of the directional derivatives is negative, the current position is selected as belonging to the shear ridge.
2. At each selected ridge position we calculate the Hessian of the analyzed shear detector S

$$H_{ij}^J = \frac{\partial^2 S}{\partial x_i \partial x_j}, \quad (5)$$

where again $x_i, x_j \in \{x, y, z\}$, and solve its eigenproblem. The minimum eigenvalue $\lambda_{\min} = \min\{\lambda_i\}$, if negative, gives the steepest decay of the shear detector S and the corresponding eigenvector $\hat{e}_n = \hat{e}(\lambda_{\min})$ indicates the direction of this decay. If the minimum eigenvalue is not negative, the location is skipped.

3. The eigenvector \hat{e}_n is perpendicular to the shear plane. In order to determine the direction of the shear we use the fact that the vector of the curl of the analyzed vector field (current density \vec{J} for \vec{B} or vorticity $\vec{\omega}$ for \vec{v}), which can be easily obtained, is perpendicular to \hat{e}_n . Therefore, the direction of the sheared component \hat{e}_s is

$$\hat{e}_s = \hat{e}_n \times \hat{w}, \quad (6)$$

where $\hat{w} = \vec{w}/|\vec{w}|$ and $\vec{w} = \nabla \times \vec{u}$.

4. Next, we perform the interpolation of all three components of the analyzed vector field, u_x , u_y , and u_z along the vector \hat{e}_n within a distance of several cell sizes (e.g., $s = -20h, \dots, 20h$, where s is the distance in the units of cell size h), and project the resulting vectors on the direction of shear component \hat{e}_s

$$u_s(s) = \hat{e}_s \cdot \vec{u}(s\hat{e}_n). \quad (7)$$

We use a piecewise quintic Hermite interpolation which preserves continuity of the first and second derivatives (see, e.g., Dougherty et al. 1989).

5. At this point we perform fitting of a function $f(s) = u_a \tanh[(s - s_0)/\delta] + u_0$ to the obtained profile $u_s(s)$. The estimated value u_a corresponds to the amplitude of the sheared component of vector field and u_0 is the uniform component across the shear plane, but perpendicular to the guide field.
6. Along the normal direction we can also project other quantities, for example, in the case of the tearing mode we estimate the transverse component of magnetic field $B_n(s) = \hat{e}_n \cdot \vec{B}(s\hat{e}_n)$ or Alfvén speed $v_A(s) = \hat{e}_n \cdot \vec{v}_A(s\hat{e}_n)$. By averaging them within the local current sheet, i.e. within the interval $s \in (-\delta, \delta)$ of the fitted function, we can get the mean value of the transverse component of magnetic field $\langle B_n \rangle$ and the Alfvén speed $\langle v_A \rangle$, which is necessary to estimate the specific Lundquist number S_δ .
7. Finally, in order to estimate the length of the current sheet, i.e. the longitudinal dimension of the local sheet plane, we project the shear detector S along the vector parallel to the reconnecting component of magnetic field, $S(s) = S(s\hat{e}_r)$, and analyze the decay of S along s . We measure the distance l between points where S drops to a half of its central value treating l as the longitudinal length of the current sheet.

The procedure described above allows us to estimate the thickness δ and the longitudinal dimension l of a shear region at its arbitrary position, to determine the direction of the shear (e.g. the reconnecting component in case of magnetic field) \hat{e}_s , and to estimate other related to growth rate parameters, such as the mean transverse and guide magnetic components, B_n and B_g , respectively, the relative strength of the transverse component $\xi = B_n/B_a$, the maximum current density $J_m = B_p^2/\delta$, or the specific Lundquist number

$S_\delta = v_A\delta/\eta$, in the case of tearing mode, or the shear strength ΔU and Alfvén speed v_A in the case of Kelvin–Helmholtz instability.

In the left panel of Figure 1 we show a sketch of a shear region (with arbitrary orientation) with vector field lines of the opposite polarization (red and blue) with the local reference frame used to project the field components on three axes \hat{e}_s , \hat{e}_n , and \hat{e}_g , corresponding to shear, transverse and guide components. For the case of magnetic shear, an extracted profiles of shear (reconnecting) $B_s(s)$, transverse $B_n(s)$, and guide $B_g(s)$ components (blue, orange, and green respectively) along the direction normal to the current sheet are shown in the right panel of Figure 1. This panel also shows the fitting of the shear component (red dashed line) with estimated parameters B_a , B_0 and δ , which values are shown in the title together with the estimated stabilizing parameter ξ .

3.3. Extracted Parameters for Tearing Instability

The estimation of the growth rate of tearing mode in fluid simulations is not trivial. First of all, it is necessary to detect the locations of current sheets using, for example, the algorithm presented in the previous subsection. Once it is done, one have to estimate the length l and thickness δ of the local sheet. Within the local sheet we can estimate the strength of the transverse and reconnecting components, B_n and B , respectively, in order to determine ξ , and the specific Lundquist number S_δ . It is especially difficult to characterize the local perturbations. Usually we have a situation where several perturbation waves of different amplitudes and travelling in different directions are present in the analyzed region. It is enough, however, to determine the limit on the minimum wavelength k_{min} , which can be obtained from the already estimated length of the current sheet, i.e. $k_{min} \approx L/l$. The maximum wavelength is determined by the resolution of the simulation, $k_{max} \approx L/h$.

3.4. Extracted Parameters for Kelvin–Helmholtz Instability

The Kelvin–Helmholtz instability is analyzed in a similar manner as the tearing mode. Here we determine the positions of the velocity shear using the algorithm describe in this section. Once the shear region is detected, its thickness δ and longitudinal dimension l are estimated. These two parameters allow up to estimate the permitted range of perturbation wave numbers. In order to determine the growth rate of the Kelvin–Helmholtz instability in each detected region, we calculate the shear velocity $\Delta U = v_s(s_0 + \delta) - v_s(s_0 - \delta)$ from the interpolated transverse component of velocity, where s_0 and

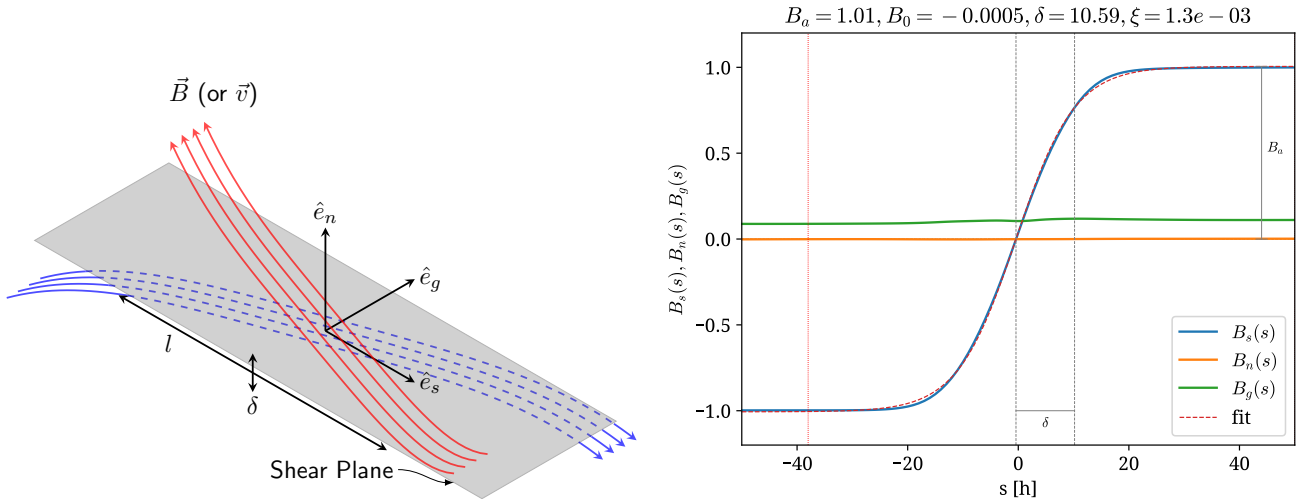


Figure 1. *Left:* Sketch of a shear region with the local reference frame indicating directions of the shear \hat{e}_s , transverse (normal) \hat{e}_n , and guide components \hat{e}_g of the analyzed vector field (magnetic field \vec{B} or velocity \vec{v}). The length l of the shear region and its thickness δ are determined along \hat{e}_s and \hat{e}_n axes, respectively. *Right:* Example profiles of the shear (reconnecting), transverse and guide components of magnetic field (B_s , B_n , and B_g , respectively) projected on the direction normal to current sheet in one of the selected points of the detected current sheet. The estimated parameters of the fitting of the reconnecting component $B_s(s)$ are shown in the title. The horizontal scale is in the units of the effective cell size h .

δ are obtained from the fitting of the function $f(s)$ (see step 5 in §3.2). Similarly to tearing mode, we estimate the mean Alfvén speed v_A across the shear region. In this way we build a vector of samples for the shear width δ , the shear velocity ΔU , and the Alfvén speed v_A , necessary to verify the stability conditions and estimate the growth rate from Eq. 3 which statistics we analyze in the next section.

4. ANALYSIS AND RESULTS

4.1. Tearing instability analysis

Before we estimate the growth rate of tearing mode instability, we should analyze the properties of current sheet in the system, which influence the growth rate. From Eq. 1 we see, that the growth rate increases with the decrease of the current sheet thickness δ and the increase of the perturbation wavelength k . These two quantities also determine the instability condition $k\delta < 1$. Therefore, we will analyze them first.

In the left plot of Figure 2 we show the distribution of current sheet thicknesses δ in all detected current sheet cells in the model with sound speed $a = 1.0$ at times $t = 0.1, 1.0, 3.0, 5.0$, and 7.0 . Two vertical lines correspond to the effective cell size $h = 1/2048$ (left) and the initial current sheet thickness $\delta_{ini} = 3.16 \times 10^{-3}$. We see that at initial times two populations of the samples corresponding current sheet regions, the first one which is dominating, where its thickness broadens to values several times larger than the initial thickness δ_{ini} , and the second one characterized by very broad current sheets

with δ comparable to a fraction of the unit length L (see the green line in Fig. 2 corresponding to $t = 3.0$). This population of broad current sheets seems to be transient, since at $t = 5.0$ (red line in Fig. 2) it is significantly decreased. For $t \geq 5.0$, the distributions are not characterized by two populations anymore, and they shift to much smaller values of δ , becoming at a fraction of the detected current sheet samples comparable or below the effective cell size h , indicating a sharp change of magnetic field orientation across the sheet (only two cells to change the polarization of magnetic field lines) and probably related to turbulent dynamics near the sheet plane. On the other side, the number of current sheet samples quickly decays with the value of δ , indicating that thick current sheets are not too common in the system anymore.

Respectively, in the right plot of Figure 2 we show the evolution of distribution of the current sheet region lengths for the same model at the same times. As expected, initially we have one current sheet plane, extended over the whole box. This is indicated by a significant number of samples of $l \approx 1.0$ at $t = 0.1$. However, we can also see, that a less significant population of samples show lengths being a fraction of L . We would interpret them as the points belonging to parts of the current sheet already mostly deformed, since using our analysis, we cannot determine if these points belong to the same or separated current sheets. What is important, that this population increases with time, as seen at times $t = 1.0$ and 2.0 (orange and green curves, respec-

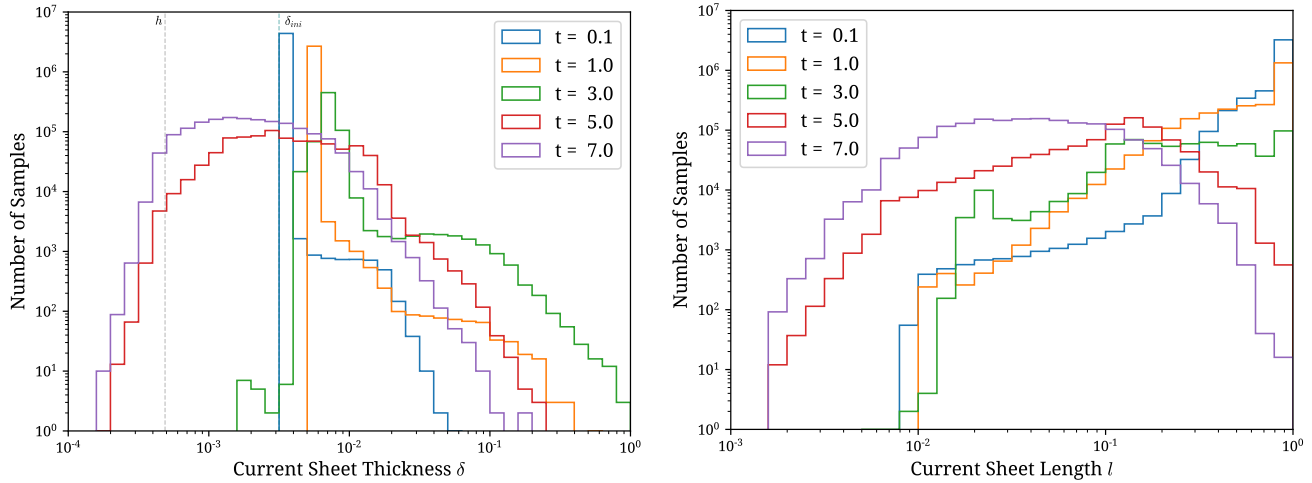


Figure 2. Statistics of the current sheet thickness δ (left) and length l (right) for the model with sound speed $a = 1.0$ with explicit resistivity $\eta = 10^{-5}$ and effective cell size $h = 1/2048$ for different evolution moments, $t = 0.1, 1.0, 3.0, 5.0, 7.0$ (blue, orange, green, red, and purple, respectively). The right vertical dashed line (teal) shows the initial thickness of current sheet $\delta_{ini} = 3.16 \times 10^{-3}$, and the left line (grey) shows the effective grid size h .

tively). At later times, $t > 3.0$, nearly all points belong to significantly shorted current sheet regions than initially, with values mostly spread between $l = 10^{-2}$ and 10^{-1} at $t = 7.0$ (purple line).

Analyzing Figure 2 we can deduce, that tearing mode should be a preferential instability at initial times, which are characterized by relatively thin and extended current sheets with $\delta \approx 0.005 - 0.05$ and $k = 1/l \approx 1 - 10$ resulting in instability condition $k\delta \lesssim 0.5 < 1$. At later times the thickness decreases to values $\delta \approx 0.001 - 0.1$, which should support development of the tearing mode, however, the fragmentation or deformations of the current sheet decrease significantly the length of the current sheet regions increasing somewhat the condition $k\delta$. Nevertheless, we should remember, that initial perturbations were imposed at very small scales $k > 100$, resulting in a relatively inefficient development of tearing mode during the first stage, reduced even more by initial broadening of the current sheet thickness. At later times the situation could improve, since the developed turbulence generate fluctuations at larger scales and helps to decrease the thickness of current sheet.

The analysis above did not respond clearly, if initially the turbulence can be generated by tearing mode. At later times, the turbulence develops in regions where current sheet is thinner, potentially increasing the growth rate of the instability. At the same time, however, it is possible that the same turbulence generates component of magnetic field normal to current sheet, which, according to Equation 4, may suppress the instability. In order to analyze the stabilizing effect of this component, we show the correlations between the normalized transverse component of mag-

netic field $\xi = B_n/B$ and the specific Lundquist number $S_\delta = v_A \delta / \eta$ in Figure 3 for two moments, $t = 3.0$ (left panel) and $t = 7.0$ (right panel). The red line, corresponding to the relation $\xi = S_\delta^{-3/4}$, divides the plot into two regions: one below the line, where ξ has negligible effect, and another above the line, where the stabilization by ξ takes place and is significant. From the distribution shown in the left panel we see, that most of the detected cells are unstable at $t = 3.0$ with values of S_δ concentrated slightly below the value of 10^3 and the stabilization parameter ξ spreading up to value 10^{-2} . A partial stabilization in the upper tail, i.e. for $\xi \approx 10^{-2} - 10^{-1}$, already takes place. It has a characteristic increase in the direction of larger values of S_δ at $\xi \approx 10^{-1}$. This is probably due to the broadening of the current sheet seen in the left panel of Figure 2. The points above $\xi = 1.0$ are statistically insignificant.

At later time, $t = 7.0$, shown in the right panel of Figure 3, the situation is very different. The points of distribution are spread toward lower values of S_δ , roughly between 10^1 and 10^3 , and across many orders of magnitude along the stabilization parameter ξ , nearly up to 10^2 . We see a significant concentration of detected samples slightly above the red line dividing two stability regions. The spread along the horizontal direction should be attributed to the decrease of current sheet thicknesses due to the action of turbulence, which is also responsible for generating transverse component stabilizing tearing instability. From the distributions shown we see that the generation of ξ by turbulence cannot be ignored in any analysis of the growth rate of tearing mode. If this effect does not completely stabilize the instability, it can

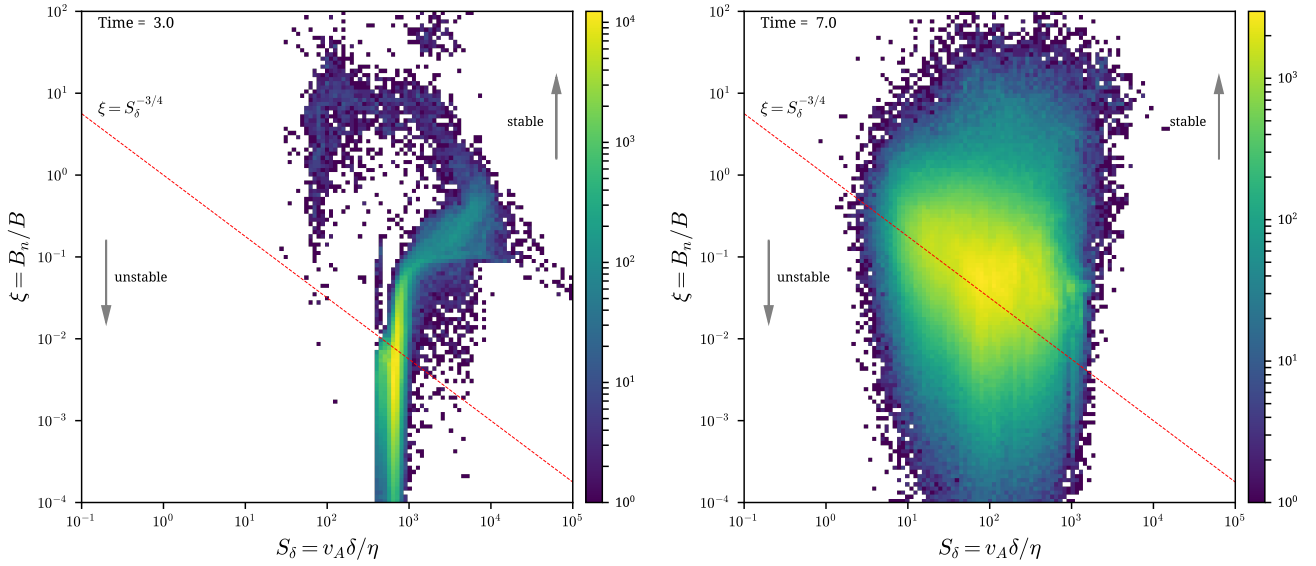


Figure 3. Correlations between the ratio of the transverse component of magnetic field to the magnetic field amplitude within the current density $\xi = B_n/B$ against the Lundquist number $S_\delta = \delta v_A/\eta$ at two evolution moments $t = 3.0$ (left) and $t = 7.0$ (right). The red dashed line divide the unstable (below) and stable (above) regions.

at least significantly suppress its growth (see the second term on the right hand side in Eq. 2).

An interesting question to ask is what is the principal direction of magnetic shear in the unstable cells at different moment, considering the presence of a guide field and weak initial perturbations. In Figure 4 we show the angular distribution of the shear measure for the unstable cells only at two moment, $t = 3.0$, and 7.0 . We notice, that at $t = 3.0$ the shear direction is still strongly concentrated along the X direction, with a spread roughly from -20° to 20° in the azimuthal and from -10° to 10° in the vertical direction, with some very rare events reaching even higher altitudes. At the final time, $t = 7.0$, we notice, that the distribution of directions, even though still concentrated along the X axis, but this time which much larger spread in both directions, azimuthal and vertical. This indicates, that the turbulence acting on the current sheet, can significantly bend it, modifying its local topology.

4.2. Kelvin–Helmholtz instability analysis

Similarly to the tearing mode analysis, we first show in Figure 5 evolution of distributions of the thickness and length of the velocity shear regions applied in order to analyze the Kelvin–Helmholtz instability. The first interesting observation from these plots is that there are no detected velocity shear regions for times $t = 0.1$ and 1.0 , or the shear strength was too weak, below the set threshold value $\Delta U_{min} = 10^{-4}$ set in the shear detection algorithm. These distributions are for all cells with detected velocity shear, not only the unstable ones. At

$t = 3.0$ we already see a number of cell belonging to a shear region of thicknesses between 2×10^{-3} and a fraction of length unit, with a peak value shifting from values below 10^{-2} for $t = 3.0$ to values larger than 10^{-2} at $t = 7.0$. Looking at the right panel of Figure 5 we see that these shear regions spread in longitudinal dimension from several cells to the length unit, indicating a generation of nearly global shear in the computational domain. Transforming these lengths into wave number indicates, that perturbations of any k , from $k = 1$ up to nearly $k \sim 1000$, may grow due to Kelvin–Helmholtz instability, if appropriate conditions are fulfilled in the local shear region. The peak value for the longitudinal dimension of shear regions is about $l \sim 0.1$, decreasing slightly for later times, corresponding to wave number of $k \sim 10$.

The most important parameter in the development of the Kelvin–Helmholtz instability is the shear strength ΔU . In the left panel of Figure 6 we show the evolution of distribution of ΔU for all cells where shear was detected (dashed lines) and only for cells which are unstable, i.e. where $\Delta U > 2v_A$. We notice, that even though shear is relatively common after $t = 3.0$, only the cell with the strongest ΔU are in fact unstable. We see that for these unstable cells the shear strength spreads between 10^{-2} to nearly 2.0 , measured in Alfvén speed v_A . At later times, the distribution peaks at values close to v_A . This plot clearly indicates, that strong shear can be generated in such systems in relatively short time.

In the right panel of Figure 6 we verify prediction for the compressible system by Miura & Pritchett (1982),

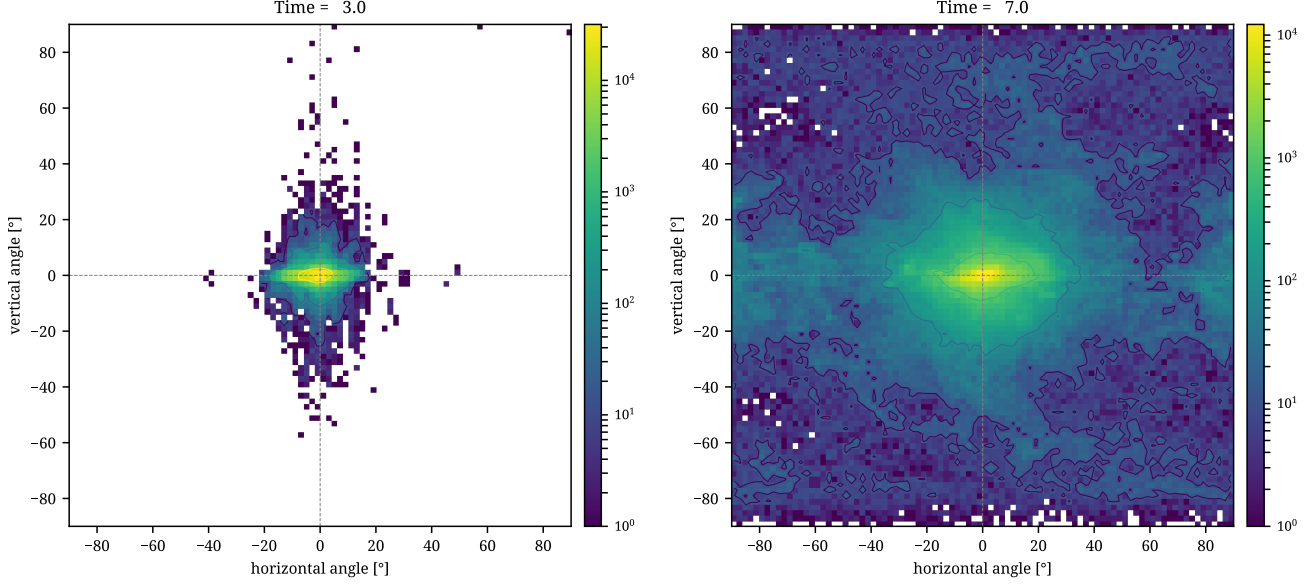


Figure 4. Distribution of the magnetic shear direction in unstable cells for the same model and moments as shown in Fig. 3. The horizontal angle corresponds to the azimuthal angle projected on the XZ plane with respect to the X axis. The vertical angle is the angle between the shear direction and the XZ plane.

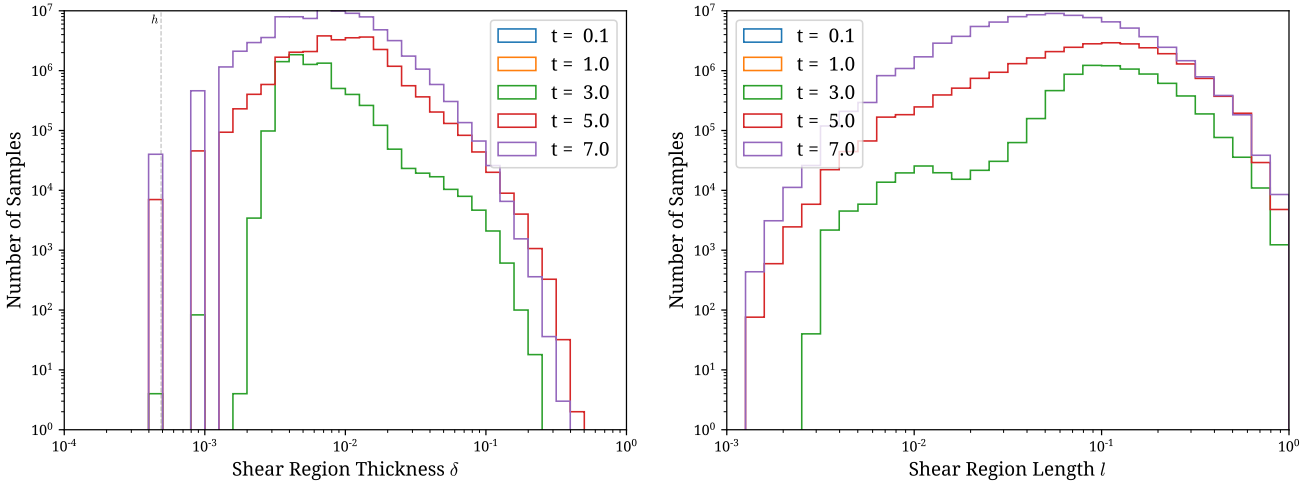


Figure 5. Statistics of the velocity shear region thickness δ (left) and length l (right) for the same model as shown in Fig. 2 at different evolution moments, $t = 0.1, 1.0, 3.0, 5.0, 7.0$ (blue, orange, green, red, and purple, respectively). Solid lines represent Kelvin–Helmholtz unstable cells only, which the dashed lines show distribution for all shear detected regions. The vertical dashed line (grey) shows the effective grid size h .

that if sonic Mach number $\mathcal{M}_s > 2.0$ or $\mathcal{M}_A < 2.0$ the instability is stabilized. We show distribution of both Mach numbers in the last snapshot of our simulation, at $t = 7.0$. Clearly, all unstable cells, have sonic Mach number $\mathcal{M}_s < 2.0$ and Alfvénic Mach number $\mathcal{M}_A > 2.0$, being in perfect agreement with the theoretical prediction.

Similarly to tearing mode analysis, we show the distribution of shear direction, this time the velocity one in Figure 7 for two moments of time, at $t = 3.0$ (left),

when the Kelvin–Helmholtz unstable cells appear, and at the final moment $t = 7.0$ (right). We see that at $t = 3.0$ the Kelvin–Helmholtz instability is still insignificant, with only around 900 unstable cells detected. However, these unstable cells have relatively large angular spread around the X direction. The velocity shear directions are scattered over all angles in both directions, azimuthal and vertical, although the statistically significant part is within 20° from the X axis, elliptically elongated in the azimuthal direction.

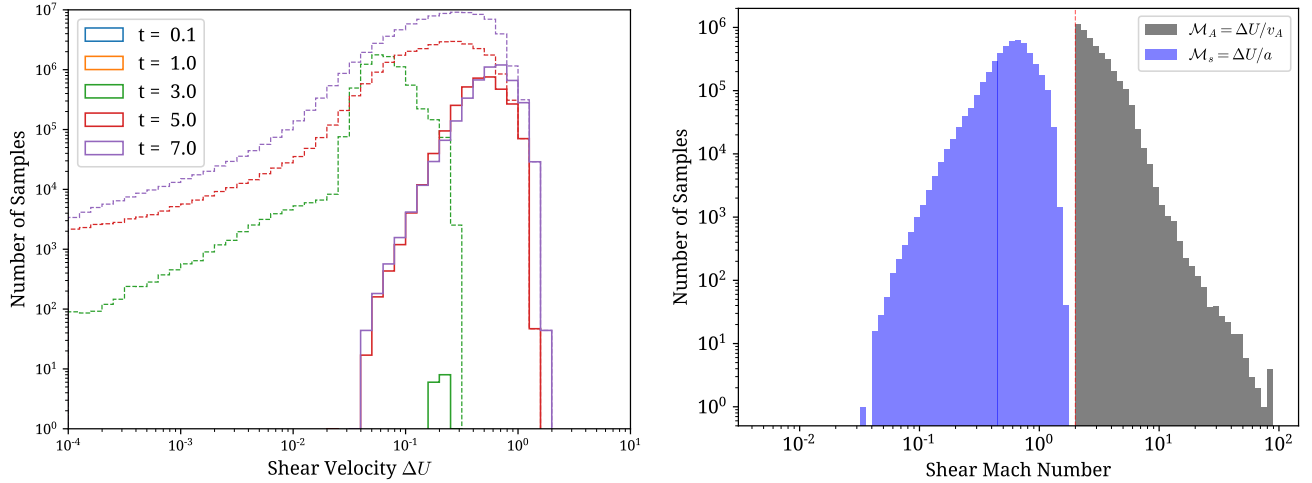


Figure 6. *Left:* Evolution of the distribution of the velocity shear strength ΔU for different times. Dashed lines correspond to all cells where shear was detected, while solid lines show only Kelvin–Helmholtz unstable cells. *Right:* Distribution of sonic (blue) and Alfvénic (grey) Mach numbers related to the velocity shear in Kelvin–Helmholtz unstable samples for model with sound speed $a = 1.0$ at $t = 7.0$. The red dashed line corresponds to Mach number equal 2.0. As predicted by [Miura & Pritchett \(1982\)](#), for all unstable cells $\mathcal{M}_s < 2$ and $\mathcal{M}_A > 2$.

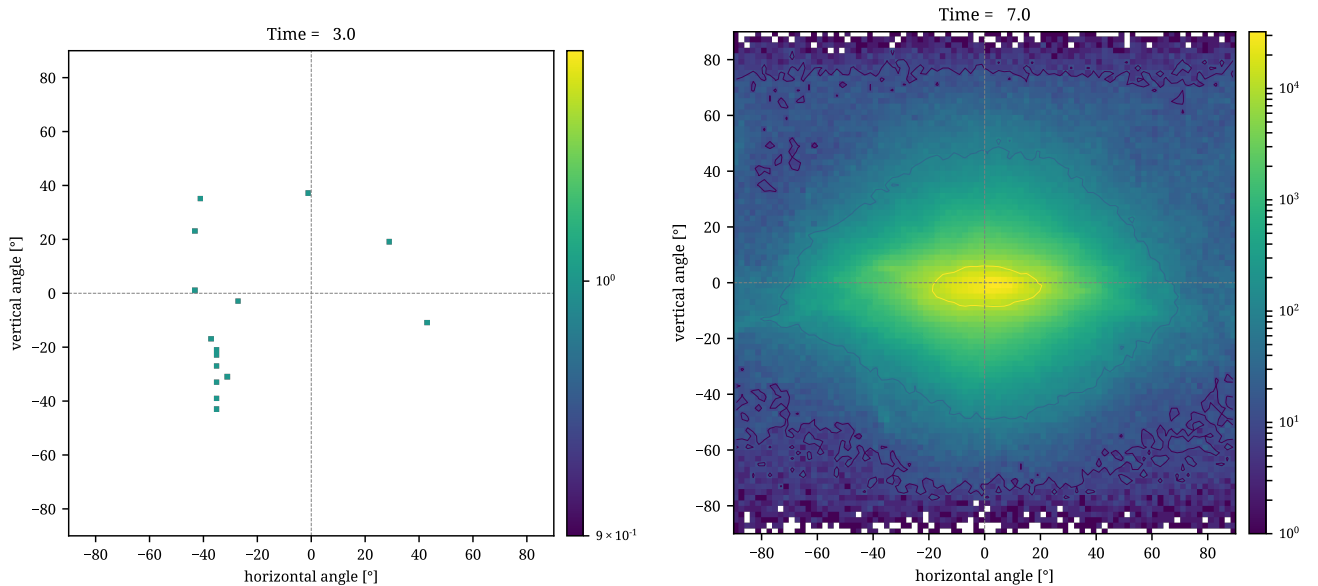


Figure 7. Distribution of the velocity shear direction in unstable cells for the same model and moments as shown in Fig. 3. The horizontal angle corresponds to the azimuthal angle projected on the XZ plane with respect to the X axis. The vertical angle is the angle between the shear direction and the XZ plane.

4.3. Evolution of the Growth Rates: Tearing vs. Kelvin–Helmholtz

Supported by the results from previous subsections, showing analysis of the factor which are important for development of both instabilities or suppress them, we can now estimate the growth rate for both instabilities, assuming the wave number k of perturbations. As we already showed, the range of possible wave numbers k for both instabilities can be estimated from distribu-

tions of the longitudinal dimension of shear regions l . In case of both instabilities, the minimum wave number $k_{min} = 1$ due to the size of the box. However, the estimated maximum wave number k_{max} is slightly different for both instabilities, with $k_{max} \approx 300$ for tearing mode and $k_{max} \approx 800$, with peak values between $k = 1$ and $k = 100$ for both. Therefore, the estimation of growth rates was done for three assumed values of perturbation wave number, $k = 1, 10, \text{ and } 100$.

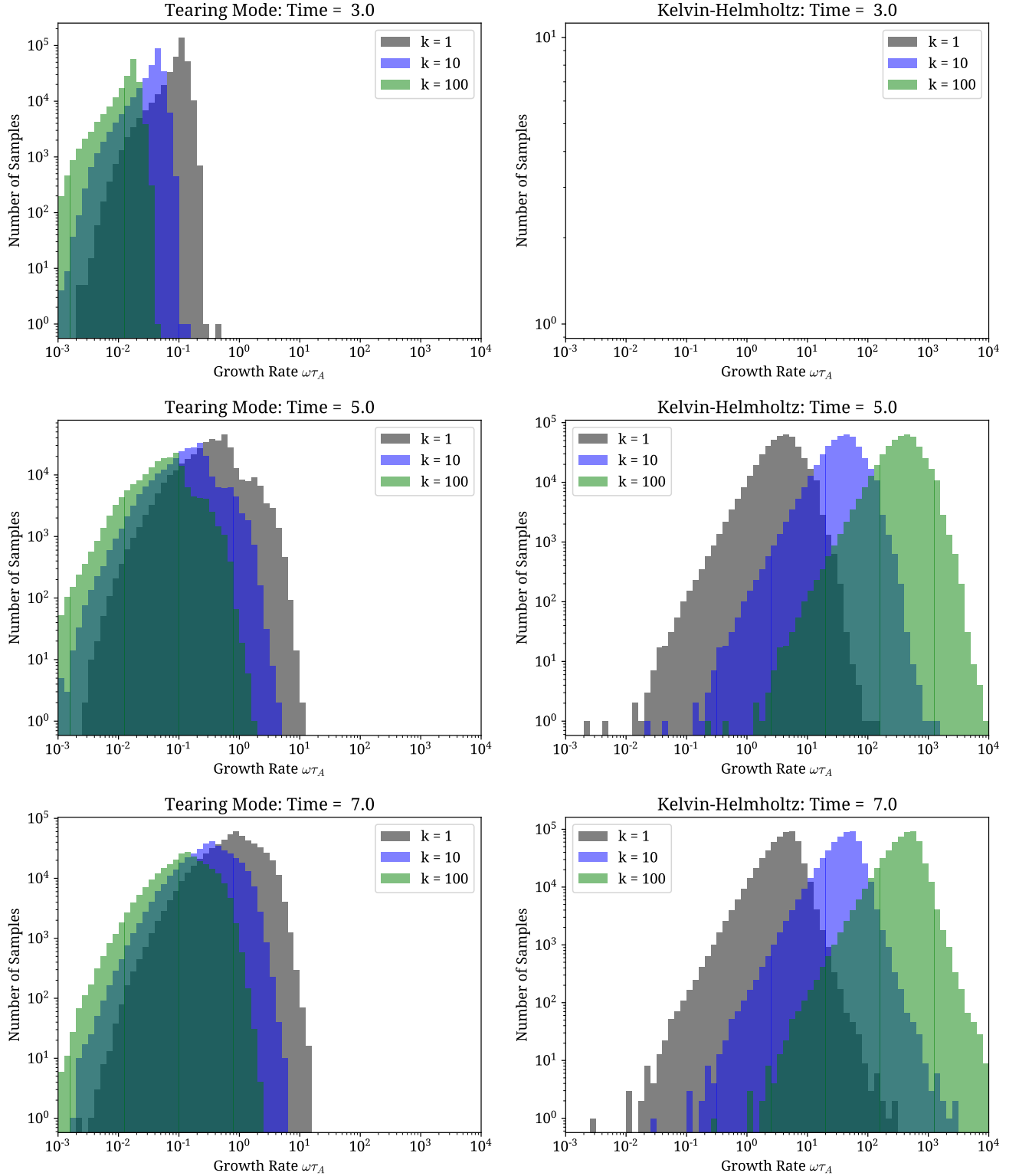


Figure 8. Evolution of the growth rates for tearing model (left column) and Kelvin–Helmholtz (right column) at three different time moments, $t = 3.0, 5.0,$ and 7.0 (upper, middle, and lower rows, respectively) for three selected wave numbers of perturbations, $k = 1, 10,$ and 100 (grey, blue, and green histograms, respectively).

In Figure 8 we show the estimated growth rate distributions for both instabilities. The statistics for tearing mode and Kelvin–Helmholtz instability are shown in the left and right column, respectively. Three different time moments were chosen, $t = 3.0$, 5.0 , and 7.0 , shown in the upper, middle, and lower rows, respectively. We see, that at earlier times, the Kelvin–Helmholtz instability is relatively negligible. The number of detected cells is orders of magnitude lower comparing to the case of tearing mode. However, even though the tearing mode is widespread, its growth rates are very small, meaning that it would need several Alfvén times to develop, considering that the initial perturbations have mostly small scales. On the contrary, the Kelvin–Helmholtz instability, even with insignificant filling factor at $t = 3.0$, can develop in a fraction of Alfvén time, since its estimated growth rates are much larger than the tearing mode ones, as seen in the right upper panel of Figure 8.

At $t = 5.0$, the number of samples of Kelvin–Helmholtz instability is comparable to the one of tearing mode (see middle row of Fig. 8). The tearing mode growth rates extend to higher values, roughly by order of magnitude, comparing to earlier time shown, $t = 3.0$. However, the Kelvin–Helmholtz growth rates extends toward both, smaller and higher values, reaching values of 10^4 for $k = 100$, three orders of magnitude higher comparing to tearing mode.

For the final moment shown, $t = 7.0$, the distributions of growth rates for both instabilities seem very similar to the one shown for $t = 5.0$. Both instabilities have slightly above 10^5 samples at peak values of distributions, however, the tearing mode peaks at growth rates $\omega\tau_A \lesssim 1$, while the Kelvin–Helmholtz instability peaks at $\omega\tau_A \gg 1$. This indicates, that if any favorable velocity shear is formed by turbulence, the instability can grow nearly instantly.

5. DISCUSSION

5.1. Limitations of our approach

Our approach in analyzing tearing and Kelvin–Helmholtz instabilities is robust, however, it has its drawbacks, which should be pointed out. First of all, in the presence of growing turbulent fluctuations, it is nearly impossible to determine the characteristics of the perturbations present in the analyzed local shear region. In order to determine the growth rate precisely, we would have to possess information about the wave number and direction of each local perturbation. In order to compensate the lack of these data, we assumed a few typical wave numbers ($k = 1, 10, 100$), and assumed direction which produce smallest growth rate (e.g., the term $\vec{k} \cdot \vec{B}$ for Kelvin–Helmholtz case).

Our results are based on the statistics extracted from the cell by cell analysis. We do not determine the individual shear regions and analyze each region separately. For example, in the case of tearing instability analysis, we have one current sheet initially crossing the whole computational box. Due to developing turbulence, this current sheet is being deformed, and eventually fragmented into a number of current sheet regions, not necessarily separated, but interlinked in a complex manner. Therefore, our analysis should be understood in terms of volume (or filling factor) rather, than individual structures. This should be kept in mind especially when interpreting the statistics of longitudinal dimensions of the shear regions.

Original derivation of the growth rate of the Kelvin–Helmholtz instability considered discontinuous velocity shear (see Chandrasekhar 1961). As a result, the growth rate depends linearly on the perturbation wave number. Later, a number of works analyzed this instability taking into account a smooth transition of velocity within the shear region, concluding the existence of the wave number k_{max} for which the growth rate is maximum, and which typically is related to the thickness of the region δ (see Ong & Roderick 1972; Walker 1981; Miura & Pritchett 1982; Chen et al. 1997; Berlok & Pfrommer 2019). This maximum growth rate is usually a fraction of the growth rate corresponding to the discontinuous shear. Still, it is much larger than the growth rates for tearing mode obtained in our analysis. They also demonstrated stabilization of the instability for $k\delta \gg 1$. In our models δ varies between 10^{-3} and 10^{-1} , which confirms that selected values of wave number k are reasonable. Nevertheless, we aim to study the effects of finite thickness of velocity shear region in the forthcoming paper.

5.2. Turbulent reconnection as a dominant process

Suggested 20 years ago, the turbulent reconnection model has gotten significant support both from subsequent numerical (see Kowal et al. 2009, 2012, 2017; Eyink et al. 2013; Oishi et al. 2015; Takamoto et al. 2015; Beresnyak 2017; Takamoto 2018), theoretical (Eyink et al. 2011; Eyink 2011, 2015; Lazarian et al. 2015, 2019), as well as observational (see Ciaravella & Raymond 2008; Sych et al. 2009, 2015; Khabarova & Obridko 2012; Lazarian et al. 2012; Santos-Lima et al. 2013; Leão et al. 2013; González-Casanova et al. 2018) studies. At the moment of its introduction the model was an alternative to the Hall-MHD models predicting Petschek X-point geometry of reconnection point, i.e., very regular type of reconnection. The later model required plasma to be collisionless, which is in contrast to the turbu-

lent one, which did not depend on any plasma microphysics and was applicable to both collisional and collisionless media. It was later understood that the X-point geometry is not tenable in realistic settings. Instead, the tearing reconnection (see Syrovatskii 1981; Loureiro et al. 2007; Bhattacharjee et al. 2009) became the main alternative scenario for the turbulent model. So far 2-dimensional simulations demonstrated fast reconnection for both MHD and kinetic regimes. Compared to earlier Hall-MHD reconnection that necessarily required collisionless plasma condition this was definitely an important improvement. The tearing reconnection shares many features with the turbulent one. For instance, Hall-MHD reconnection required a particular set of boundary conditions that was difficult to preserve in the realistic setting with the random external perturbations, not needed for tearing case.

With two reconnection processes providing fast reconnection, it is important to understand the applicability of each. It has been numerically demonstrated in Kowal et al. (2009) that including additional microscopic effects simulating enhanced plasma resistivity does not change the turbulent reconnection rate. This agrees well with the theoretical expectations in turbulent reconnection (see LV99 and Eyink (2011)), in particular with the generalized Ohm's law derived in Eyink (2015). As a result, if media is already turbulent, one does not expect to see effects of tearing reconnection. With the existing observational evidence about the turbulence of astrophysical fluids this means that the turbulent reconnection is dominant for most of the cases. For instance, we expect the turbulent reconnection to govern violation of the flux freezing in turbulent fluids. This results in reconnection diffusion that governs star formation (Lazarian et al. 2012), induces the violations of the structure of the heliospheric current sheet and the Parker spiral (Eyink 2015).

The numerical results on flux freezing violation that follows from the LV99 theory cannot be possibly explained with the tearing reconnection. This clearly demonstrates that there are situations when the turbulent reconnection is at work, while tearing reconnection is not expected.

The "pure" problem of self-driven turbulent reconnection was the focus of our study in Kowal et al. (2017). There we showed that in the absence of the external turbulence driving the turbulence develops in the reconnection region and this turbulence has the properties corresponding to the expectations of the MHD turbulence. This was in contrast to Huang & Bhattacharjee (2016) who claimed that turbulence produced in reconnection regions is radically different from the Goldreich & Srid-

har (1995) one. The properties of turbulence are important, as the LV99 magnetic reconnection and closely connected to it Richardson dispersion (Eyink et al. 2011) are proven to work in conditions where no tearing instability is expected. Therefore, if such type of turbulence is present in the reconnection regions it is expected to induce fast reconnection. The correspondence of the reconnection rates in self-driven reconnection with the expectations of the LV99 theory was demonstrated in Lazarian et al. (2015), where the results of earlier simulations, e.g. Beresnyak (2013), were analyzed.

The present paper is a step forward in understanding the process of self-induced fast reconnection. Here we explore the nature of turbulence driving in the reconnection region. If tearing mode is absolutely essential for driving turbulence, one may still argue that the actual reconnection is happening via tearing, while the turbulence is playing only an auxiliary role for the process. Our results, in fact, testify that the actual picture is very different. The process of tearing mode plays in 3D a role at the earliest stage of reconnection. As the system evolves in time the outflows induced by the reconnection region become turbulent, with Kelvin-Helmholtz instability playing the dominant role. As the reconnection grows, the region becomes more and more turbulent with the tearing instability being overtaken or even suppressed, not playing a role on the reconnection process overall.

Our simulations are performed in the high beta plasma regime and in such conditions the reconnection outflow does not induce sufficient turbulence to trigger the self-accelerating process of "reconnection instability" (see Lazarian & Vishniac 2009) though.

While the MHD simulations show a very different picture for 2D and 3D self-driven reconnection, the particles-in-cell (PIC) simulations tend to show similar tearing patterns both in 3D and 2D. One possible explanation is related to limitations of present-day PIC simulation, given that these do not present enough particles in the reconnection regions to result in developed turbulence. Therefore, in such "viscous" regime the Kelvin-Helmholtz instability is suppressed and cannot operate and the only signatures that can be seen arise from the tearing instability. In other words, the "viscous" outflow does not feel the additional degrees of freedom that would allow high Reynolds turbulent behavior to take place. Nevertheless, the high resolution PIC simulations presented by Hui Li in a reconnection review by Lazarian et al. (2019) show the signatures of developing turbulence, e.g., the Richardson dispersion of magnetic field lines was reported. Therefore, we expect that the results we now obtained with MHD modelling can be

also obtained/confirmed with very high particle number PIC simulations.

There is, however, another puzzle that is presented by the comparison of the 3D kinetic and MHD simulations. The kinetic simulations show higher reconnection rates and it is important to understand whether these differences persist for reconnection at all scales or they are just a transient feature of reconnection processes taking place for small-scale reconnection. This issue was recently addressed in Beresnyak (2018) using Hall-MHD code. The results there testify that the reconnection rates for self-driven 3D turbulent reconnection obtained with Hall-MHD gradually converge to the results obtained for the 3D MHD self-driven reconnection. This is what one expects from the theory (see LV99; Eyink et al. 2011; Eyink 2015). Nevertheless, in terms of our present study the convergence of the results obtained with MHD and Hall-MHD code testify that the results in the present paper will not change in the presence of additional plasma effects.

Our confirmation of the predictions of turbulent reconnection theory formulated in the LV99, and subsequent theoretical studies, also has bearing on the ongoing discussion of the so called "reconnection-mediated turbulence" idea presented in a number of theoretical papers (see Loureiro & Boldyrev 2017a,b; Boldyrev & Loureiro 2017, 2018; Walker et al. 2018; Mallet et al. 2017b,a; Comisso et al. 2018; Vech et al. 2018). For sufficiently large Reynolds numbers, due to both the process of "dynamical alignment" and the effect of magnetic fluctuations getting more anisotropic with the decrease of the scale, the current sheets prone to tearing instability can develop. Such changes of the turbulence at the scale λ_c in the vicinity of the dissipation scale do not change the nature of turbulent cascade, which lies on scales of the inertial range $\gg \lambda_c$. Our study is therefore suggestive that if reconnection takes place at small scales, comparable to λ_c , it will also be turbulent as demonstrated by our simulations. However, since reconnection does not happen at the larger eddies scales it is preferred to refer this hypothetical regime as "tearing-mediated turbulence" instead. The objective reality is, however, that in the reconnection community historically only bursts of reconnection was considered.

5.3. *Our advance of the field*

One of the most important results of the work on reconnection-driven turbulence is the reassurance of self-generation of turbulence in reconnection events. The other is that this turbulence follows standard Kolmogorov and Goldreich–Sridhar statistics. However, a still open issue is related to the driving mechanism

of the observed turbulent motions. What drives the turbulence in reconnection events? The literature has suggested, without any quantitative proof, that tearing modes, plasmoid instabilities, and shear-induced instabilities could mediate the energy transfer from coherent to turbulent flows.

In our numerical experiments we do not identify tearing modes, although filamentary plasmoid-like structures are present. The filling factor of these are, however, visually recognized as very small. Sheared flows, on the other hand, are present around and within the whole current sheet. As the field lines reconnect, the $\vec{v} \times \vec{B} + \vec{E}$ force increases, accelerating the plasma and creating the current sheet. This process is, in three dimensions, patchy and bursty. Therefore, the accelerated flows are strongly sheared. The statistical importance of these bursty flows is large, as we compared the velocity anisotropy of reconnecting events to that of decaying turbulence without the reversed field. Kelvin–Helmholtz instability due to the sheared velocities in reconnecting layers has already been conjectured as possible origin of turbulence by Beresnyak (2017). In the previous work, we therefore provided real evidence for the self-generated turbulence driven by the velocity shear. Here we have performed a proper analysis of the growth-rates of such instabilities.

Another consequence of the mechanism responsible for turbulence self-generation is on the statistics of perturbations. Velocity shear is a global process that occurs in regular magnetized and unmagnetized fluids. The nonlinear evolution of related instabilities, such as Kelvin–Helmholtz instability, is known to be one of the main contributors to the energy transfer rate between wave modes, i.e., the energy cascade. If the energy cascade in reconnection layers is led by similar mechanisms, it is straightforward to understand why the statistics observed resemble those of Kolmogorov-like turbulence, and Goldreich–Sridhar anisotropy scaling. In other words, our claim is that the turbulent onset and cascade in reconnection is not different to those found in regular MHD and hydrodynamic systems.

6. CONCLUSIONS

In this work we analyzed two MHD instabilities: tearing mode and Kelvin–Helmholtz, which are candidates for processes responsible for turbulence generation in spontaneous reconnection, e.g. the reconnection without externally imposed turbulent driving. The generated turbulence is due to the initially imposed weak noise present in the vicinity of the Harris current sheet. We analyzed factors important for growth of both instabilities, but also those which suppress them. The anal-

ysis presented in this work has shown important results which can be synthesized in the following:

- The region of current sheet with the presence of initial noise develops into a region with conditions favorable for development of MHD instabilities, such as tearing mode or Kelvin–Helmholtz instability. Although the tearing instability is natural for thin elongated current sheets, the conditions for Kelvin–Helmholtz instability have never been verified before in systems with stochastic reconnection.
- Evolution of stochastic reconnecting provides to formation of shear regions, both magnetic and velocity, with broad range of thicknesses and longitudinal dimensions. We estimated, that the maximum perturbation wave number is smaller for tearing mode compared to Kelvin–Helmholtz. Since the growth rate is proportional to k , it increases quicker for the later.
- Tearing instability is expected to develop at earlier stages, while, once a sufficient amplitude of turbulence is generated near the current sheet, it can be suppressed due to the presence of the transverse component of magnetic field B_n . As shown in [Somov & Verneta \(1993\)](#), for $\xi = B_n/B > S_\delta^{-3/4}$ this instability is suppressed. We demonstrate that in our models ξ can be sufficiently large to

shut the instability down in most of the simulated volume. Still, taking into account the contribution of transverse component B_n , the instability can develop with dynamical time shorter than the Alfvénic time t_A under favorable circumstances.

- Due to misalignment of the outflows from neighboring reconnection events, they can generate enough sheared flows to induce Kelvin–Helmholtz instability. The Mach numbers calculated with respect to the shear velocity ΔU satisfy necessary conditions for the instability to develop. Our analysis indicates the presence of sheared regions with broad range of amplitudes, $10^{-2} \leq \Delta U \leq 1$, and thicknesses, $10^{-3} \leq \delta \leq 0.5$. The estimated growth rates $\omega\tau_A$, larger than 10^2 for $k \geq 10$, suggest the growth of Kelvin–Helmholtz instability (within the dynamical time) much shorter than the Alfvénic time t_A itself.

G.K. acknowledges support from CNPq (no. 304891/2016-9). D.F.G. thanks the Brazilian agencies CNPq (no. 311128/2017-3) and FAPESP (no. 2013/10559-5) for financial support. A.L. acknowledges the NSF grant 1816234 and NASA TCAN 144AAG1967. E.T.V. acknowledges the support of the AAS. This work has made use of the computing facilities the Academic Supercomputing Center in Kraków, Poland (Supercomputer Prometheus at ACK CYFRONET AGH) and of the Laboratory of Astrophysics (EACH/USP, Brazil).

REFERENCES

- Alfvén, H. 1942, *Nature*, 150, 405, doi: [10.1038/150405d0](#)
- Armstrong, J. W., Rickett, B. J., & Spangler, S. R. 1995, *ApJ*, 443, 209, doi: [10.1086/175515](#)
- Beresnyak, A. 2013, ArXiv e-prints. <https://arxiv.org/abs/1301.7424>
- . 2017, *ApJ*, 834, 47, doi: [10.3847/1538-4357/834/1/47](#)
- Beresnyak, A. 2018, in *Journal of Physics Conference Series*, Vol. 1031, *Journal of Physics Conference Series*, 012001
- Berlok, T., & Pfrommer, C. 2019, *MNRAS*, 485, 908, doi: [10.1093/mnras/stz379](#)
- Bhattacharjee, A., Huang, Y.-M., Yang, H., & Rogers, B. 2009, *Physics of Plasmas*, 16, 112102, doi: [10.1063/1.3264103](#)
- Boldyrev, S., & Loureiro, N. F. 2017, *ApJ*, 844, 125, doi: [10.3847/1538-4357/aa7d02](#)
- Boldyrev, S., & Loureiro, N. F. 2018, in *Journal of Physics Conference Series*, Vol. 1100, *Journal of Physics Conference Series*, 012003
- Chandrasekhar, S. 1961, *Hydrodynamic and hydromagnetic stability* (Oxford)
- Chen, Q., Otto, A., & Lee, L. C. 1997, *J. Geophys. Res.*, 102, 151, doi: [10.1029/96JA03144](#)
- Chepurnov, A., Burkhart, B., Lazarian, A., & Stanimirovic, S. 2015, *ApJ*, 810, 33, doi: [10.1088/0004-637X/810/1/33](#)
- Chepurnov, A., & Lazarian, A. 2010, *ApJ*, 710, 853, doi: [10.1088/0004-637X/710/1/853](#)
- Ciaravella, A., & Raymond, J. C. 2008, *ApJ*, 686, 1372, doi: [10.1086/590655](#)
- Comisso, L., Huang, Y. M., Lingam, M., Hirvijoki, E., & Bhattacharjee, A. 2018, *ApJ*, 854, 103, doi: [10.3847/1538-4357/aaac83](#)
- Dougherty, R. L., Edelman, A. S., & Hyman, J. M. 1989, *Mathematics of Computation*, 52, 471–494, doi: [10.1090/S0025-5718-1989-0962209-1](#)
- Eyink, G., Vishniac, E., Lalescu, C., et al. 2013, *Nature*, 497, 466, doi: [10.1038/nature12128](#)

- Eyink, G. L. 2011, *PhRvE*, 83, 056405, doi: [10.1103/PhysRevE.83.056405](https://doi.org/10.1103/PhysRevE.83.056405)
- . 2015, *ApJ*, 807, 137, doi: [10.1088/0004-637X/807/2/137](https://doi.org/10.1088/0004-637X/807/2/137)
- Eyink, G. L., Lazarian, A., & Vishniac, E. T. 2011, *ApJ*, 743, 51, doi: [10.1088/0004-637X/743/1/51](https://doi.org/10.1088/0004-637X/743/1/51)
- Furth, H. P., Killeen, J., & Rosenbluth, M. N. 1963, *Physics of Fluids*, 6, 459, doi: [10.1063/1.1706761](https://doi.org/10.1063/1.1706761)
- Goldreich, P., & Sridhar, S. 1995, *ApJ*, 438, 763, doi: [10.1086/175121](https://doi.org/10.1086/175121)
- González-Casanova, D. F., Lazarian, A., & Cho, J. 2018, *MNRAS*, 475, 3324, doi: [10.1093/mnras/sty006](https://doi.org/10.1093/mnras/sty006)
- Greco, A., Chuychai, P., Matthaeus, W. H., Servidio, S., & Dmitruk, P. 2008, *Geophys. Res. Lett.*, 35, L19111, doi: [10.1029/2008GL035454](https://doi.org/10.1029/2008GL035454)
- Huang, Y.-M., & Bhattacharjee, A. 2016, *ApJ*, 818, 20, doi: [10.3847/0004-637X/818/1/20](https://doi.org/10.3847/0004-637X/818/1/20)
- Jacobson, A. R., & Moses, R. W. 1984, *PhRvA*, 29, 3335, doi: [10.1103/PhysRevA.29.3335](https://doi.org/10.1103/PhysRevA.29.3335)
- Khabarova, O., & Obridko, V. 2012, *ApJ*, 761, 82, doi: [10.1088/0004-637X/761/2/82](https://doi.org/10.1088/0004-637X/761/2/82)
- Kowal, G., Falceta-Gonçalves, D. A., Lazarian, A., & Vishniac, E. T. 2017, *ApJ*, 838, 91, doi: [10.3847/1538-4357/aa6001](https://doi.org/10.3847/1538-4357/aa6001)
- Kowal, G., Lazarian, A., Vishniac, E. T., & Otmianowska-Mazur, K. 2009, *ApJ*, 700, 63, doi: [10.1088/0004-637X/700/1/63](https://doi.org/10.1088/0004-637X/700/1/63)
- . 2012, *Nonlinear Processes in Geophysics*, 19, 297, doi: [10.5194/npg-19-297-2012](https://doi.org/10.5194/npg-19-297-2012)
- Lazarian, A. 2005, in *American Institute of Physics Conference Series*, Vol. 784, *Magnetic Fields in the Universe: From Laboratory and Stars to Primordial Structures.*, ed. E. M. de Gouveia dal Pino, G. Lugones, & A. Lazarian, 42–53
- Lazarian, A., Esquivel, A., & Crutcher, R. 2012, *ApJ*, 757, 154, doi: [10.1088/0004-637X/757/2/154](https://doi.org/10.1088/0004-637X/757/2/154)
- Lazarian, A., Eyink, G., Jafari, A., et al. 2019, *Physics of Plasmas*
- Lazarian, A., Eyink, G., Vishniac, E., & Kowal, G. 2015, *Philosophical Transactions of the Royal Society of London Series A*, 373, 20140144, doi: [10.1098/rsta.2014.0144](https://doi.org/10.1098/rsta.2014.0144)
- Lazarian, A., & Vishniac, E. T. 1999, *ApJ*, 517, 700, doi: [10.1086/307233](https://doi.org/10.1086/307233)
- Lazarian, A., & Vishniac, E. T. 2009, in *Revista Mexicana de Astronomía y Astrofísica Conference Series*, Vol. 36, *Magnetic Fields in the Universe II: From Laboratory and Stars to the Primordial Universe*, ed. A. Esquivel, J. Franco, G. García-Segura, E. M. de Gouveia Dal Pino, A. Lazarian, S. Lizano, & A. Raga, 81–88
- Leão, M. R. M., de Gouveia Dal Pino, E. M., Santos-Lima, R., & Lazarian, A. 2013, *ApJ*, 777, 46, doi: [10.1088/0004-637X/777/1/46](https://doi.org/10.1088/0004-637X/777/1/46)
- Loureiro, N. F., & Boldyrev, S. 2017a, *PhRvL*, 118, 245101, doi: [10.1103/PhysRevLett.118.245101](https://doi.org/10.1103/PhysRevLett.118.245101)
- . 2017b, *ApJ*, 850, 182, doi: [10.3847/1538-4357/aa9754](https://doi.org/10.3847/1538-4357/aa9754)
- Loureiro, N. F., Schekochihin, A. A., & Cowley, S. C. 2007, *Physics of Plasmas*, 14, 100703, doi: [10.1063/1.2783986](https://doi.org/10.1063/1.2783986)
- Mallet, A., Schekochihin, A. A., & Chandran, B. D. G. 2017a, *Journal of Plasma Physics*, 83, 905830609, doi: [10.1017/S0022377817000812](https://doi.org/10.1017/S0022377817000812)
- Mallet, A., Schekochihin, A. A., & Chandran, B. D. G. 2017b, *MNRAS*, 468, 4862, doi: [10.1093/mnras/stx670](https://doi.org/10.1093/mnras/stx670)
- Matthaeus, W. H., & Lamkin, S. L. 1985, *Physics of Fluids*, 28, 303, doi: [10.1063/1.865147](https://doi.org/10.1063/1.865147)
- . 1986, *Physics of Fluids*, 29, 2513, doi: [10.1063/1.866004](https://doi.org/10.1063/1.866004)
- Miura, A., & Pritchett, P. L. 1982, *J. Geophys. Res.*, 87, 7431, doi: [10.1029/JA087iA09p07431](https://doi.org/10.1029/JA087iA09p07431)
- Oishi, J. S., Mac Low, M.-M., Collins, D. C., & Tamura, M. 2015, *ApJL*, 806, L12, doi: [10.1088/2041-8205/806/1/L12](https://doi.org/10.1088/2041-8205/806/1/L12)
- Ong, R. S. B., & Roderick, N. 1972, *Planet. Space Sci.*, 20, 1, doi: [10.1016/0032-0633\(72\)90135-3](https://doi.org/10.1016/0032-0633(72)90135-3)
- Padoan, P., Juvela, M., Kritsuk, A., & Norman, M. L. 2009, *ApJL*, 707, L153, doi: [10.1088/0004-637X/707/2/L153](https://doi.org/10.1088/0004-637X/707/2/L153)
- Parker, E. N. 1957, *J. Geophys. Res.*, 62, 509, doi: [10.1029/JZ062i004p00509](https://doi.org/10.1029/JZ062i004p00509)
- Petschek, H. E. 1964, *NASA Special Publication*, 50, 425
- Santos-Lima, R., de Gouveia Dal Pino, E. M., & Lazarian, A. 2013, *MNRAS*, 429, 3371, doi: [10.1093/mnras/sts597](https://doi.org/10.1093/mnras/sts597)
- Santos-Lima, R., Lazarian, A., de Gouveia Dal Pino, E. M., & Cho, J. 2010, *ApJ*, 714, 442, doi: [10.1088/0004-637X/714/1/442](https://doi.org/10.1088/0004-637X/714/1/442)
- Servidio, S., Dmitruk, P., Greco, A., et al. 2011, *Nonlinear Processes in Geophysics*, 18, 675, doi: [10.5194/npg-18-675-2011](https://doi.org/10.5194/npg-18-675-2011)
- Somov, B. V., & Verneta, A. I. 1993, *SSRv*, 65, 253, doi: [10.1007/BF00754510](https://doi.org/10.1007/BF00754510)
- Sweet, P. A. 1958, *The Observatory*, 78, 30
- Sych, R., Karlický, M., Altyntsev, A., Dudík, J., & Kashapova, L. 2015, *A&A*, 577, A43, doi: [10.1051/0004-6361/201424834](https://doi.org/10.1051/0004-6361/201424834)
- Sych, R., Nakariakov, V. M., Karlicky, M., & Anfinogentov, S. 2009, *A&A*, 505, 791, doi: [10.1051/0004-6361/200912132](https://doi.org/10.1051/0004-6361/200912132)
- Syrovatskii, S. I. 1981, *ARA&A*, 19, 163, doi: [10.1146/annurev.aa.19.090181.001115](https://doi.org/10.1146/annurev.aa.19.090181.001115)
- Takamoto, M. 2018, *MNRAS*, 476, 4263, doi: [10.1093/mnras/sty493](https://doi.org/10.1093/mnras/sty493)
- Takamoto, M., Inoue, T., & Lazarian, A. 2015, *ApJ*, 815, 16, doi: [10.1088/0004-637X/815/1/16](https://doi.org/10.1088/0004-637X/815/1/16)

Vech, D., Mallet, A., Klein, K. G., & Kasper, J. C. 2018, ApJL, 855, L27, doi: [10.3847/2041-8213/aab351](https://doi.org/10.3847/2041-8213/aab351)

Walker, A. D. M. 1981, Planet. Space Sci., 29, 1119, doi: [10.1016/0032-0633\(81\)90011-8](https://doi.org/10.1016/0032-0633(81)90011-8)

Walker, J., Boldyrev, S., & Loureiro, N. F. 2018, PhRvE, 98, 033209, doi: [10.1103/PhysRevE.98.033209](https://doi.org/10.1103/PhysRevE.98.033209)